ADVANCED FUNCTIONAL MATERIALS
www.afm-journal.de

Materials Views
www.MaterialsViews.com

Self-Assembly of Nanostructured, Complex, Multication Films via Spontaneous Phase Separation and Strain-Driven Ordering

*Sung Hun Wee, Yanfei Gao, Yuri L. Zuev, Karren L. More, Jianyong Meng, Jianxin Zhong, George M. Stocks, and Amit Goyal**

Spontaneous self-assembly of a multication nanophase in another multication matrix phase is a promising bottom-up approach to fabricate novel, nanocomposite structures for a range of applications. In an effort to understand the mechanisms for such self-assembly, complimentary experimental and theoretical studies are reported to first understand and then control or guide the self-assembly of insulating $BaZrO_3$ (BZO) nanodots within $REBa_2Cu_3O_{7-\delta}$ (RE = rare earth elements including Y, REBCO) superconducting films. The strain field developed around BZO nanodots embedded in the REBCO matrix is a key driving force dictating the self-assembly of BZO nanodots along REBCO *c*-axis. The size selection and spatial ordering of BZO self-assembly are simulated using thermodynamic and kinetic models. The BZO self-assembly is controllable by tuning the interphase strain field. REBCO superconducting films with BZO defect arrays self-assembled to align in both vertical (REBCO *c*-axis) and horizontal (REBCO *ab*-planes) directions result in the maximized pinning and J_c performance for all field angles with smaller angular J_c anisotropy. The work has broad implications for the fabrication of controlled self-assembled nanostructures for a range of applications via strain-tuning.

1. Introduction

Epitaxial nanostructured composite films containing self-assembled, ordered arrays of nanodots/nanorods/nanopillars of one type of complex, multication material embedded in another multication ceramic material have broad potential use in a range of applications such as multiferroics, magnetoelectrics, thermoelectrics, ultrahigh density storage, and high temperature (high-T_c) superconductors.[1–6] Such nanocomposite films with different overall composition, concentration, feature size, and spatial ordering of the embedded nanophase can produce a number of novel and unprecedented properties which are not exhibited in individual materials or phases comprising the composite films. For high-T_c superconductor applications, $REBa_2Cu_3O_{7-\delta}$ (RE = rare earth elements including Y, REBCO) nanocomposite films containing self-assembled stacks of insulating $BaZrO_3$ (BZO) nanodots/nanorods have been demonstrated for enhanced vortex pinning.[5–8] Incorporation of cubic, perovskite-structured, BZO phase into REBCO spontaneously forms vertical nanocolumns aligned to REBCO *c*-axis. Formation of similar columnar structures has been also demonstrated by the incorporation of other complex materials into REBCO, such as $BaSnO_3$, Ba_2RETaO_6, and Ba_2RENbO_6.[9–11] Effective pinning via these defects results in substantial enhancement of the critical current density (J_c) in high magnetic fields particularly when the applied magnetic field is parallel to the orientation of the aligned defects.[5–11] However, there is a lack of or gap in fundamental understanding of the mechanism of such self-assembly. Using the REBCO superconductor system as an example, we report on our combined experimental and theoretical efforts to understand the thermodynamic effects and kinetic processes that dictate the strain-mediated, self-assembly in REBCO+BZO composites. We further demonstrate control of such self-assembly via strain-tuning to obtain more desirable nano-defect configurations to maximize vortex-pinning and J_c for all magnetic field angles in REBCO+BZO nanocomposites.

The self-assembly of BZO nanodots/nanorods in REBCO matrix is governed by both thermodynamics and kinetic processes driven by minimization of local and long-range strain field arising from the lattice mismatch of ≈8% between BZO and REBCO phases. As schematically illustrated in **Figure 1**a, the self-assembly of BZO nanodots/nanorods in REBCO matrix occurs by simultaneous phase separation and strain ordering

Dr. S. H. Wee, Prof. Y. Gao, Dr. K. L. More, Dr. J. Zhong, Dr. G. M. Stocks, Dr. A. Goyal
Materials Science and Technology Division
Oak Ridge National Laboratory
Oak Ridge, TN 37831, USA
E-mail: goyala@ornl.gov
Prof. Y. Gao, J. Meng
Department of Materials Science and Engineering
University of Tennessee
Knoxville, TN 37996, USA
Dr. Y. L. Zuev
Department of Physics
University of Tennessee
Knoxville, TN 37996, USA

DOI: 10.1002/adfm.201202101

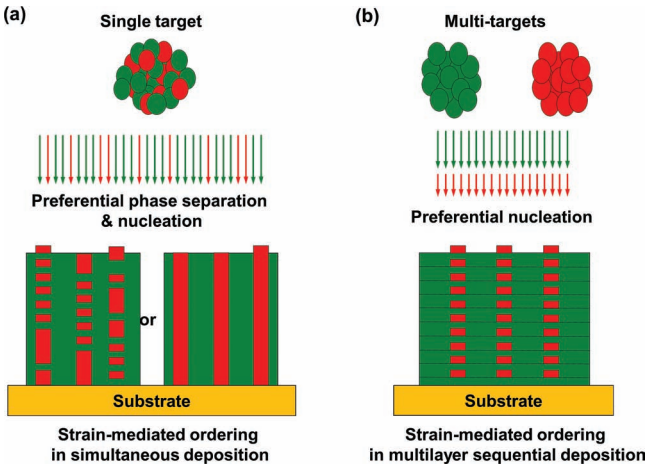

Figure 1. Schematic diagram illustrating self-assembly of one complex nanophase material within another complex matrix material phase: a) via simultaneous phase separation and phase ordering mechanism by deposition from a single target consisting of a mixture of two materials; and b) via conventional phase ordering mechanism based on sequential deposition using multiple targets. In (a), columnar structures formed by either self-assembled stacks of nanodots/nanorods or continuous nanopillars as is schematically illustrated.

(SPSO) process during in situ pulsed laser deposition (PLD) using a single REBCO target containing a few volume% (vol%) of BZO phase. Instead of vertical stacks of nanodots/nanorods, a nanophase in the form of continuous nanopillars[1,3] can be produced, as also illustrated in Figure 1a. The process is similar to but different from the conventional self-assembly process reported earlier in semiconductor heteroeptaxial systems constructed by sequential multilayer deposition as also schematically illustrated in Figure 1b.[12] In both cases, local strain field around a nanophase stemming from the misfit strain (ε_s) caused by the lattice mismatch with a matrix is considered a key driving force for the vertical alignment into columnar arrays perpendicular to the surface of the substrate. However, there is a radical difference between the two processes in terms of kinetics. In the heteroepitaxial semiconductor system, nanodots of one material form on the surface of another material, and the embedded nanostructures tune the subsequent nanodots by a stress-mediated preferential nucleation mechanism. The vertical alignment should happen even if there is a relatively smaller strain field since a multilayer sequential deposition process provides the sufficient time for a vertical alignment process, and no phase separation process is needed. In contrast, for BZO self-assembly by SPSO process, the phase separation and vertical alignment of nanodots/nanorods in a matrix phase should occur at the same time because the two materials are simultaneously ablated and delivered to the substrate. Another major difference is that our system attains an equilibrium feature size while the equilibrium state in sequential deposition in semiconductor quantum dots is an infinitely long wavelength. In addition, kinetic processes involving diffusion, deposition, and phase separation are competing in the SPSO process. Hence, relatively larger strain is required to provide sufficient kinetic energy for the self-assembly, and the size selection and vertical ordering can be tuned by energetic and kinetic parameters—an aspect that will be explored experimentally in this work. Indeed, it has been considered that lattice mismatches in the range of ≈5–12% generate adequate local strain fields required for the self-assembly by SPSO process.[13] The mismatches below this range do not result in enough misfit strains and hence no *c*-axis oriented self-assembly occurs and instead, the formation of randomly oriented, epitaxial nanoparticles (for example, in the case of CeO_2 and RE_2O_3 embedded in REBCO matrix) is favored. At very large mismatches above this range, formation of nonepitaxial, random oriented nanoparticles such as that observed for $BaCeO_3$ in YBCO matrix (with a lattice mismatch of ≈13%) is observed.

2. Results and Discussion

The SPSO mechanism is first considered from a thermodynamic point of view. The size of the nanodots/nanorods (hereafter denoted simply as nanodots) can be determined thermodynamically by energetic competition between increase in phase boundary energy and relaxation of elastic strain energy. When a thin layer of REBCO and BZO phases is deposited on an elastic substrate into periodic lateral patterns, the lattice mismatch between these two phases induces a superficial deformation field in the film-substrate system. With the reduction of the spacing between BZO phases, the phase boundary energy increases, but the elastic strain energy decreases and eventually reaches a plateau value when the period is comparable to the film thickness. Consequently, the total free energy combining both phase boundary and elastic relaxation will reach a minimum that selects an energetically favorable feature size. Quantitatively, consider a regular array of BZO columns with period L, thin film thickness d, and phase size l, so that the BZO concentration is $c_0 = l^2/\ L^2$ (**Figure 2**a). Using the classic Eshelby cut-and-weld method,[14,15] the reduction of elastic energy is equal to one half of the work done by the biaxial traction applied on the phase boundary with the magnitude of this traction being $M\varepsilon_T$, where M is the biaxial modulus and ε_T is the transformation strain of BZO.

$$\varepsilon_T = \frac{a_{BZO} - a_{YBCO}}{a_{BZO}} \approx 8\%. \quad (1)$$

The change of the total free energy per unit area (in *ab* plane) as a function of period L is

$$\Delta G = \frac{4dl}{L^2}\gamma - \frac{2}{L^2}\int\int M\varepsilon_T u_n d\,A \quad (2)$$

where u_n is the displacement normal to the phase boundary, and the surface integral is performed over the phase boundary. The comparison between the phase boundary energy and the elastic energy defines a dimensionless parameter,

$$\beta = \frac{4\gamma}{M\varepsilon_T^2 d} \quad (3)$$

using $\gamma = 1$ J m^{-2}, $M = 430$ GPa, $\varepsilon_T = 0.08$, and d of about several nanometers gives rise to β ranging from 0.1 to 1. In the finite element calculations, the bottom of the substrate is fixed, the

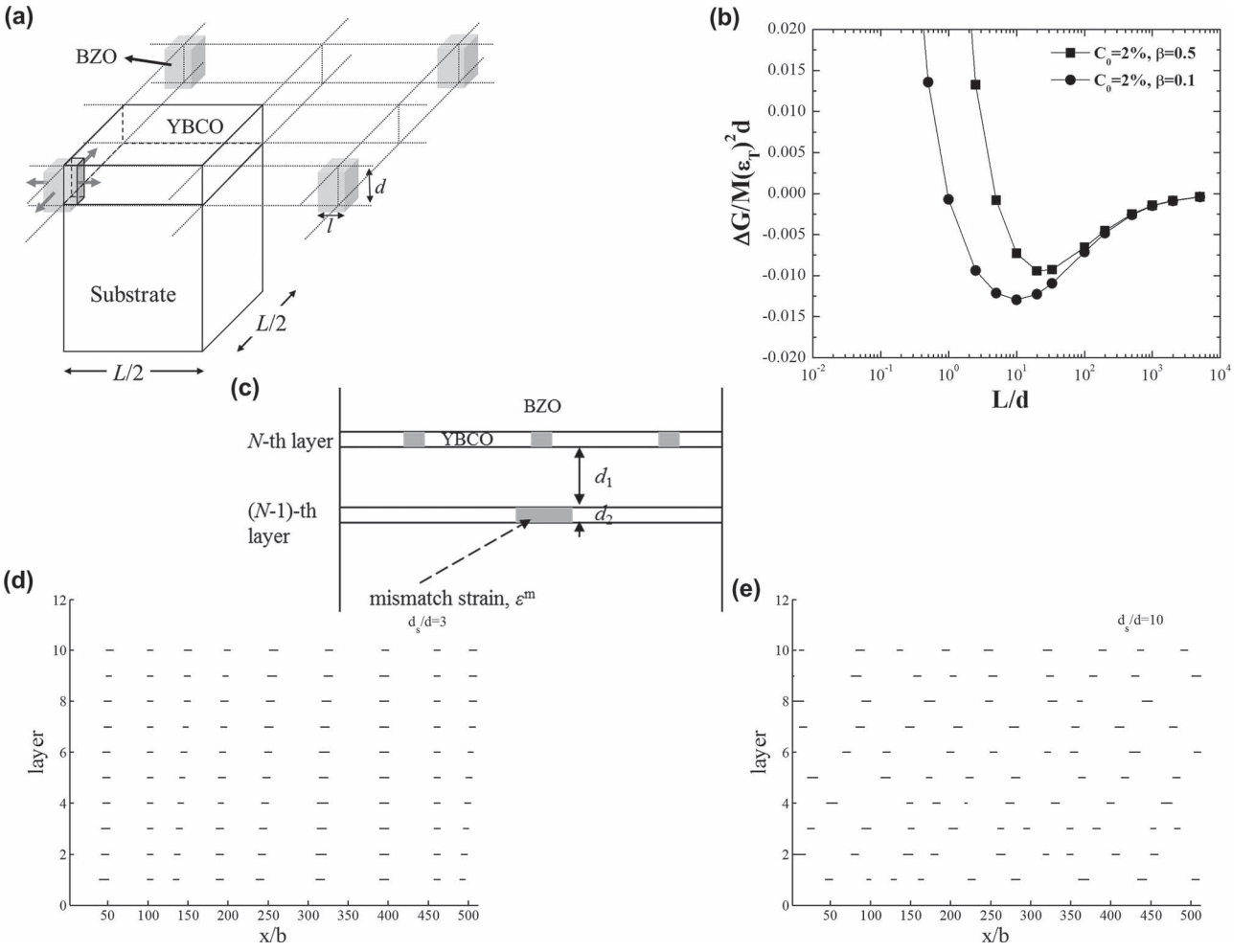

Figure 2. a) Schematic diagram illustrating the elastic interaction in the REBCO+BZO composite with a regular array of BZO columns with period *L*, thin film thickness *d*, and the phase size *l*. b) Finite element calculations determine the phase-boundary displacement when subjected to normal tractions and the elastic potential energy in Equation (2). The change of the normalized free energy is plotted against the ratio of pattern period to film thickness. The energy minimum corresponds to an energetically favorable periodic pattern with a period of about tens of nanometers. c) Schematic illustration of the sequential multilayer growth of spacer layers and REBCO-BZO co-deposited layers. d) Vertical alignment of BZO phase can be achieved when the spacer layer is thin, e.g., $d_s/d = 3$. e) No vertical ordering can be found for $d_s/d = 10$. Note that for sequential deposition, there is always horizontal alignment of BZO nanodots regardless of a degree of vertical orderliness.

surface of the film is free, and the remaining four boundaries are all applied symmetric boundary conditions. The competition between the phase boundary energy and the elastic interaction results in an energy minimum, which can be reached if sufficient time is permitted. This energetic ground state corresponds to a pattern period, L_{eq} of about tens of nanometers as shown in Figure 2b.

The reason why *d* is several nanometers is due to kinetic effects. During the deposition process, only atoms in a few marginal layers (i.e., a thickness of *d*) are mobile and contribute to the kinetic self-assembly process. In the SPSO process, at beginning of the film growth, mobile atoms in the first several layers self-assemble into a periodic pattern as in Figure 2a to minimize the total free energy which comprises the free energy of mixing, the phase boundary energy, and the elastic interaction energy. With sufficient time, a stable feature size is realized based upon these competing energetic considerations. In subsequent deposition, the two phases will form patterns that vertically grow on the previously, kinetically frozen periodic patterns. A weak driving force for vertical ordering is derived from the phase boundary energy, since a vertically ordered pattern minimizes the total phase boundary area (as opposed to a random pattern). Our previous kinetic Monte Carlo work[16] demonstrates that in a wide range of deposition rates and temperatures, such a vertical pattern is indeed kinetically favored, but the degree of ordering can be destroyed or significantly affected by thermal noise. A strong contribution to the vertical ordering is the elastic strain field due to the embedded nanostructures (Figure 1a).

We have developed a phase-field model to simulate the kinetic process of the strain-driven self-assembly process. This kinetic model allows us to study the kinetic processes of phase separation and surface diffusion, and to investigate the completion of size-selection due to self-elastic interaction and vertical ordering due to elastic interaction with embedded patterns. In

the SPSO process, the embedded pattern will guide the subsequent self-assembly process, thus enabling desirable vertical ordering and replication of BZO nanostructures. In a phase-field model,[17] the phase boundary is treated by a continuous change of concentration, so that book-keeping efforts are completely removed compared to the sharp-interface front-tracking model. In the model problem shown in Figure 2a, we consider the concentration evolution in the topmost layer. For simplicity, the concentration variation through the thickness direction in each layer is assumed to be constant. The total free energy per unit thickness is

$$G = \int_{A_N} \left[g(C) + h(\nabla C)^2 \right] dA + E_{el}$$

where g(C) is the free energy of mixing (taken as a double-well form to ensure phase separation), the phase boundary energy is quadratic in the concentration gradient, and the last term of E_{el} is the elastic potential energy, given by

$$E_{el} = \frac{1}{2} \int_{A_N} c_{ijkl} \varepsilon_{ij}^{T} \varepsilon_{kl}^{surf} \, dA - \int_{A_N} \varepsilon_{ij}^{T} \sigma_{ij}^{\dagger} \, dA$$

where ε_{kl}^{surf} is the strain caused by the concentration variation in the topmost layer itself. We denote σ_{ij} and ε_{ij}^{T} as the stress and strain caused by the embedded patterns. The transformation strain field is thus given by $\varepsilon_{ij}^{T} = \varepsilon_T \delta_{ij} C(\mathbf{x},t)$, where C is the BZO concentration field. Considering a two-dimensional pattern and based on the results in Zhang et al.,[18] we can derive the surface strain field due to an embedded rectangular inclusion,

$$\varepsilon_{xx}^{\dagger} = \varepsilon_T \frac{2(1+\nu)(1-2\nu)}{\pi(1-\nu)} \left\{ \tan^{-1}\left(\frac{x-x_1}{d_s}\right) - \tan^{-1}\left(\frac{x-x_2}{d_s}\right) - \tan^{-1}\left(\frac{x-x_1}{d_s+d}\right) + \tan^{-1}\left(\frac{x-x_2}{d_s+d}\right) \right\}$$

where the inclusion ranges from x_1 to x_2 and from d_s to $d_s + d$. Similarly, we can derive the strain field for the three-dimensional case. It is found that the distribution of the residual strain caused by the embedded pattern is similar to the embedded concentration field. The residual strain magnitude is roughly proportional to d/L and exponentially decays as the increase of d_s/l. Therefore, one can tune concentration field and these geometric parameters to tune the effectiveness of vertical ordering.

Using the classic nonequilibrium thermodynamics, the functional derivative of the free energy with respect to the concentration gives the chemical potential, $\mu = \delta G/\delta C$. Following the Cahn–Hilliard procedure, the final diffusion equation, named as a modified Cahn–Hilliard equation, was derived,

$$\frac{\partial C}{\partial t} = \frac{M}{\Lambda^2} \nabla^2 \left(\frac{\partial g}{\partial C} - 2h\nabla^2 C + \frac{E \varepsilon_T d}{1-\nu} \left(\varepsilon_{\alpha\alpha}^{surf} + \varepsilon_{\alpha\alpha}^{\dagger} \right) \right)$$

where Λ is the atomic density on the surface. This modified Cahn–Hilliard equation incorporates the gradient of concentration of nanophases as a function of time during the SPSO process and describes the self-assembly process well. The simulation result demonstrates that the processes of phase separation and size selection occur very fast, but it takes a very long time to reach an equilibrium state of perfect spatial ordering. It is also found that a large lattice mismatch strain, slow deposition rate, large surface diffusivity, and thin spacer layer will promote the formation of well-ordered BZO nanostructures in both vertical and lateral directions. To understand the effect of d_s/d on the self-assembly, we can assume that the self-assembly of BZO in SPSO process is an equivalent system to a multilayered REBCO/BZO with extremely thin space layer thickness of REBCO ($d_s/d \leq 3$) grown by sequential deposition process. As schematically illustrated in Figure 2c, in this case, we consider the pattern formation in the N^{th} layer due to the presence of the $(N\text{-}1)^{th}$ layers. Figures 2d, e show representative simulation results where a length b characterizes the phase boundary width. When the spacer is very thin ($d_s/d \leq 3$) (Figure 2d), strain field generated from embedded BZO nanodots in the bottom layer influences BZO nanodots in the new layer, and as a result, these are inclined to grow on top of the embedded BZO phases and forms nanocolumns along vertical direction. If the space layer is relatively thicker ($d_s/d \geq 10$), however, the vertical alignment does not occur because of an exponential decay of the residual strain field with increasing d_s/d, as shown in Figure 2e. Note that the theoretical estimation of d_s/d value determining the occurrence of the direct self-assembly can be different from those experimentally determined (although the trend is qualitatively the same), since the strains caused by the embedded, kinetically frozen patterns are a strong function of average concentration and the ratio of d/L.

The simulation results imply that we can control experimentally the degree of vertical ordering of BZO nanodots by tuning d_s/d ratio and as a result, the pinning and J_c performance for the samples. To verify this, we grew the multilayer structured $[NdBCO_{xu.c.}/BZO_{yu.c.}] \times N$ films with different unit cell (u.c.) thicknesses of NdBCO and BZO layers and the number of layer, N. The T_c and J_c values at 77 K, self-field (sf) for the samples are summarized in Table S1 (Supporting Information). The number of layers, N, was controlled to have a similar film thickness of ≈500–700 nm so as to exclude the thickness effect on J_c. The T_c values of the samples are in the range of 89.5–92 K but have no particular correlation with the thickness of BZO pseudo-layer. **Figure 3** shows angular dependent J_c, $J_c(\theta)$, at 77 K, 1 T for the multilayer samples with different d_{NdBCO}/d_{BZO} ratios. These films exhibit distinctively different $J_c(\theta)$ behavior because of BZO defects with different alignment and orderliness. The J_c data of a pure NdBCO film (0.7 μm) is also included in the figure for comparison. Note that the film also has a peak for $H||c$ due to vertically oriented grain boundaries which are originated from the IBAD-MgO template.[19] Also, some defective nature of the film suppresses an intrinsic pinning along the ab-planes and consequently, no sharp J_c peak for $H||ab$.[19] A multilayer film with the largest ratio of $d_{NdBCO}/d_{BZO} = 84$, $[NdBCO_{3u.c.}/BZO_{0.1u.c.}] \times 165$, shows no improved performance and the $J_c(\theta)$ similar to that for the pure NdBCO film. No vertical alignment of BZO nanodots in the film is anticipated due to the high d_{NdBCO}/d_{BZO} ratio. In addition, the enhancement in the pinning due to BZO nanodots randomly distributed in the film should be also negligible because of very thin BZO layer (≈0.1 unit cell, 0.42 Å) that can only produce a few BZO nanoparticles with small diameters. In contrast, the multilayer films with the smaller ratios in the range of $9.3 < d_{NdBCO}/d_{BZO} \leq 28$, such as $[NdBCO_{1u.c.}/BZO_{0.3u.c.}]$, $[NdBCO_{3u.c.}/BZO_{0.3u.c.}]$, and

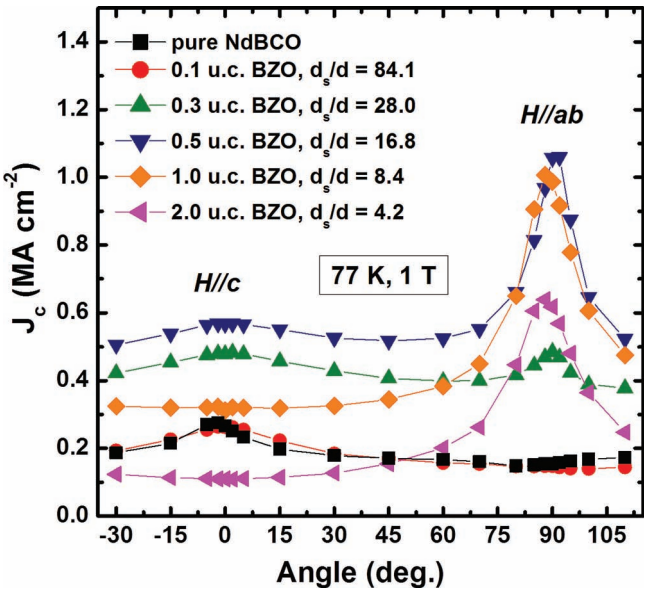

Figure 3. Angular dependent J_c at 77 K, 1 T for [$NdBCO_{xu.c.}/BZO_{yu.c.}$] × *N* multilayer samples with different BZO layer thicknesses from 0.1 to 2 unit cells, while NdBCO layer thickness is fixed to 3 unit cells.

[$NdBCO_{3u.c.}/BZO_{0.5u.c.}$] samples, show the improved J_c performance with a broad peak for $H||c$ indicating the presence of the *c*-axis correlated pinning centers that should be attributed to vertically aligned BZO nanodots as simulated in Figure 2d. One can also observe that compared to [$NdBCO_{3u.c.}/BZO_{0.3u.c.}$], the film with thinner NdBCO layer, [$NdBCO_{1u.c.}/BZO_{0.3u.c.}$], shows a stronger peak for $H||c$ and a reduction of J_c with a dip for $H||ab$ due to the stronger ordering and higher density of BZO defect arrays in the vertical direction by reducing the NdBCO space layer thickness as expected (see Figure S1, Supporting Information). For [$NdBCO_{3u.c.}/BZO_{0.5u.c.}$] multilayer film, an additional enhancement with a sharp J_c peak for $H||ab$ is observed, implying that BZO defects are aligned horizontally as well. The multilayer deposition process can induce the horizontal ordering regardless of the strain field effect, which does not occur in NdBCO+BZO samples prepared by the SPSO process using NBCO+BZO mixed targets. When the BZO pseudo-layer thickness is too thin, BZO nanodots have small sizes and wide horizontal inter-distances between them and as a result, the ordering of BZO nanodots and its effect on the $J_c(\theta)$ should be less significant. As the BZO layer grows thicker, BZO nanodots are more closely adjacent and then, the ordering effect should be prominent, and finally, continuous, planar BZO thin layer forms as further increasing the layer thickness. Indeed, we observed the $J_c(\theta)$ behavior caused by such a trend with BZO layer thickness. The multilayer samples with BZO layers thicker than 0.5 unit cell such as [$NdBCO_{3u.c.}/BZO_{1u.c.}$] and [$NdBCO_{3u.c.}/BZO_{2u.c.}$], only show sharp J_c peaks for $H||ab$ presumably due to the presence of the planar BZO defect arrays. These samples do not show the peak for $H||c$ caused by vertical alignment of BZO nanodots despite their smaller d_{NdBCO}/d_{BZO} ratios of 8.4 and 4.2. This result indicates that smaller d_{NdBCO}/d_{BZO} ratio leading to stronger vertical ordering is no more valid when the BZO layer thickness becomes too thick. This result also implies that the vertical ordering in REBCO+BZO films via the SPSO process should not occur when BZO doping concentration is too high. Formation of planar, continuous BZO layers was reported from YBCO films with higher BZO concentration such as 50 mol% YBCO + 50 mol% BZO.[20]

To identify BZO defect structures inside the films resulting in such different pinning and $J_c(\theta)$ behavior, the samples were examined by transmission electron microscopy (TEM). **Figure 4** shows cross-sectional TEM images for [$NdBCO_{3u.c.}/BZO_{2u.c.}$] and [$NdBCO_{3u.c.}/BZO_{0.5u.c.}$] multilayer samples. Dark contrast spots/lines in the images represent the BZO nanophase in the forms of nanodot/nanorod arrays. As shown in Figures 4a,b, the sample with 2.0 u.c. BZO layer contains a number of semi-continuous BZO nanodot arrays highly ordered along the *ab*-planes. Such planar arrays of BZO nanodots lead to strong *ab*-plane correlated pinning and thereby enhance J_c for $H||ab$ as shown in Figure 3. Figures 4c,d show the images of the sample with 0.5 u.c. BZO layer. Based on the $J_c(\theta)$ behavior of the sample, BZO nanodots are expected to be aligned in both *c*-axis and *ab*-plane of the film. Indeed, we observed a defect structure which contains BZO nanodots likely aligned to both directions. A low magnification image of the sample (Figure 4c) shows BZO nanodot arrays aligned along the *ab*-plane although the orderliness and the density of the arrays are much less than

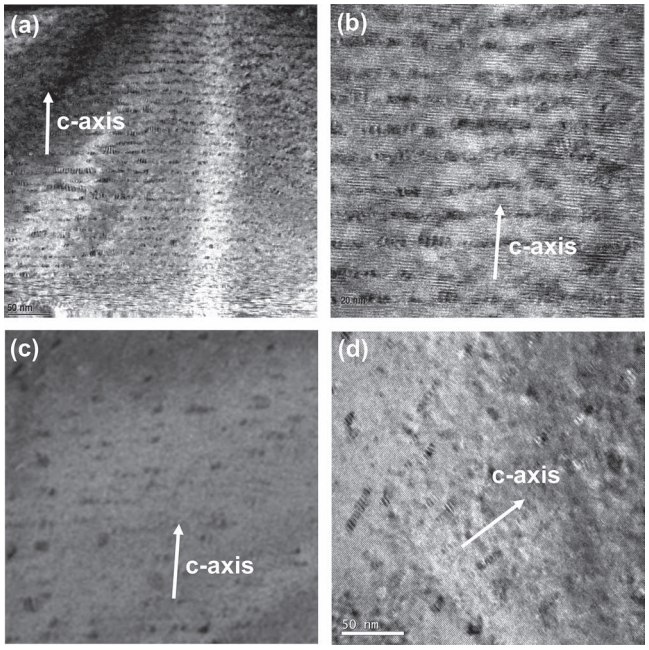

Figure 4. Cross-sectional TEM micrographs of NdBCO films with BZO pseudo-layer thicknesses of 2 and 0.5 u.c. a,b) Low and high magnification images of a [$NBCO_{3u.c.}/BZO_{2u.c.}$] multilayer film which has semi-continuous BZO nanodot arrays along the *ab*-planes. From the TEM images, the thickness of the semicontinuous BZO was estimated to be in the range of ≈19–30 Å, corresponding to ≈4.6–7.6 BZO unit cells. This is close to the nominal BZO thickness (2 unit cells) given the discontinuity of the BZO pseudo-layer. The NdBCO spacer layer was estimated to have a thickness ranging from 45 to 64 Å corresponding to ≈3.8–5.5 unit cells. The d_{NdBCO}/d_{BZO} ratio was calculated to be in the range of 1–4 which is close to the nominal value of 4.2. c,d) Low and high magnification TEM images of a [$NBCO_{3u.c.}/BZO_{0.5u.c.}$] multilayer film where BZO nanodots appear to be aligned to both directions of the *c*-axis and the *ab*-planes.

those in the sample with 2 u.c. BZO layer. On the other hand, a higher magnification TEM image (Figure 4d) taken from the same specimen shows a number of short BZO nanocolumns generally oriented to the *c*-axis. Such a hybrid nature of BZO defect structure is effective to enhance the pinning for the both field directions of $H||c$ and $H||ab$ as shown in Figure 3.

Although the sample with 0.5 u.c. BZO layer has a hybrid BZO defect structure giving rise to the best pinning and $J_c(\theta)$ performance among the NBCO/BZO multilayer samples, the *c*-axis correlated pinning and resulting J_c for $H||c$ are still much smaller than what we achieved in NdBCO+2%-BZO films with a high density of BZO columnar defects strongly ordered to the *c*-axis via SPSO process. This is because the d_{NdBCO}/d_{BZO} ratio of the film is still much larger that for the NdBCO+BZO, so that the vertical ordering of BZO nanodots in the sample is not as strong as that achieved from the NdBCO+BZO film. If NdBCO films have similar BZO columnar arrays as those obtained in the NdBCO+BZO film while sustaining BZO defect arrays along the *ab*-planes simultaneously, the sample with such a hybrid defect structure should result in higher overall $J_c(\theta)$ for all angular orientations and reduced J_c angular anisotropy determined by $J_c(H||ab)/J_c(H||c)$. Controlled introduction of BZO defects to be preferentially aligned to both *c*-axis and *ab*-planes of the film was realized by the deposition of multilayer structured films comprised of a NdBCO+BZO layer and a BZO pseudo-layer with the optimized layer thickness, $[(NdBCO+2\%\text{-}BZO)_{3u.c.}/BZO_{0.5u.c.}] \times N$. Cross-sectional TEM images for this sample are shown in **Figure 5**. As intended, BZO nanodots are highly ordered in both directions of *c*-axis and *ab*-planes of the film, as denoted by white and gray colored arrows. Since the imaging conditions that bring out the *c*-axis correlated and the *ab*-correlated BZO defects are slightly different, dark contrast due to the defects aligned to the *ab*-planes is more clearly seen in a different image of the same specimen taken from different imaging conditions as shown in Figure 5b.

Figure 6a shows $J_c(\theta)$ measured at 77 K, 1 T for the sample with such a hybrid BZO defect structure. The $J_c(\theta)$ for the NdBCO+2vol% BZO (≈0.7 μm) and $[NdBCO_{3u.c.}/BZO_{0.5u.c.}]$ multilayer samples are also included for the comparison. The $[(NdBCO+2\%BZO)_{3u.c.}/BZO_{0.5u.c.}]$ hybrid film shows superior pinning characteristics that result in much smaller J_c anisotropy with significantly improved J_c over entire magnetic field angles. J_c at $H||ab$ and $H||c$ for this sample are comparable to the highest values obtained from each of the NdBCO+BZO and NdBCO/BZO multilayer films, respectively, indicating a massive improvement of J_c for one field orientation without loss of J_c at the other field orientation, which significantly reduce J_c anisotropy. This film also has the minimum J_c with respect to the field-orientation, J_c^{min}, of 0.9 MA cm^{-2}, which is much larger than 0.51 MA cm^{-2} for the NdBCO+BZO and 0.39 MA cm^{-2} for the NdBCO/BZO multilayer sample. Figure 6b displays J_c ($H||c$) versus J_c ($H||ab$) for all films containing different BZO defect arrays. This plot visually shows J_c anisotropy as well as variation of J_c at both field directions from the sample to the sample. It is clearly seen that the $[(NdBCO+BZO)_{3u.c.}/BZO_{0.5u.c.}]$

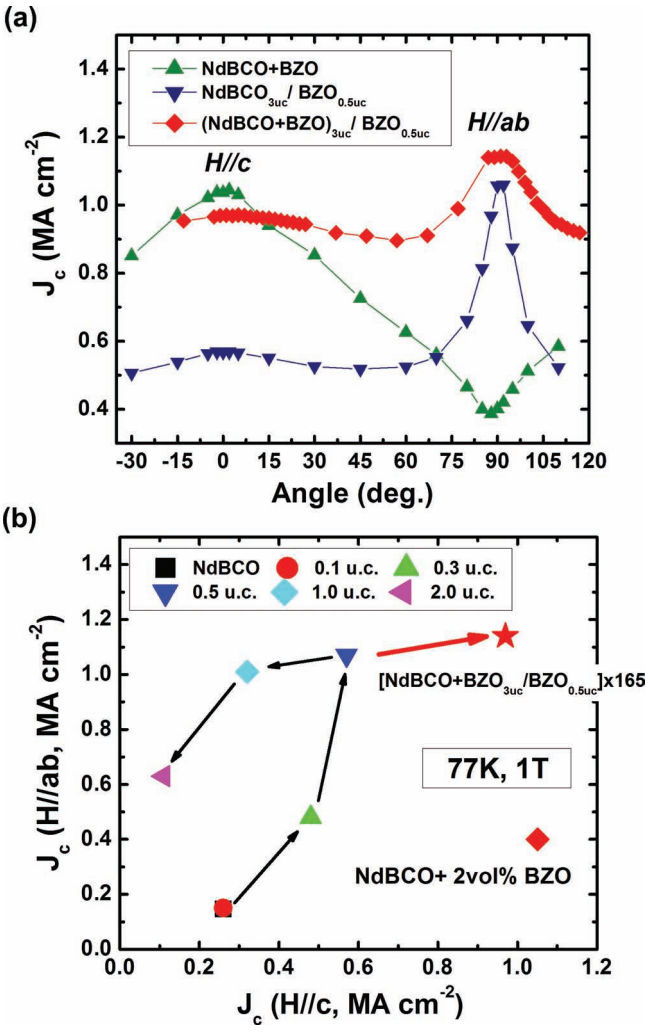

Figure 6. a) Angular dependent J_c at 77 K, 1 T for [(NdBCO+2%-BZO)/BZO] × 165 multilayer film (≈0.6 μm) with a hybrid BZO defect structure. For comparison, the J_c data of NdBCO+2%-BZO (≈0.7 μm) and NdBCO/BZO multilayer (≈0.6 μm) films are also included in the figure. b) J_c ($H||c$) vs J_c ($H||ab$) at 77 K, 1 T for all samples that include pure NdBCO, NBCO+2%-BZO, NdBCO/BZO, and (NdBCO+BZO)/BZO multilayer samples.

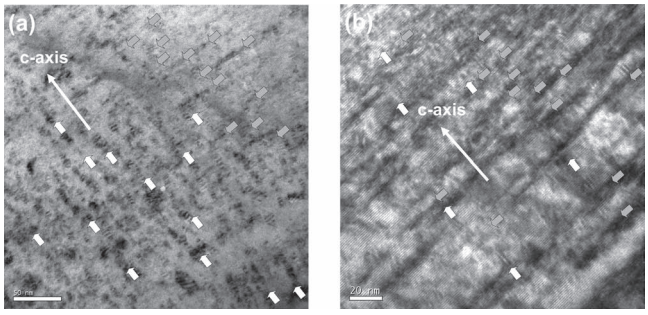

Figure 5. Cross-sectional TEM micrographs of $[(NdBCO+2\%BZO)_{3u.c.}/BZO_{0.5u.c.}] \times 165$ film. a) The image shows semicontinuous BZO nanodot or nanorods aligned parallel to both the *c*-axis and the *ab*-planes of the film. b) An image taken of the same TEM specimen at a different imaging condition highlighting BZO defects aligned parallel to the *ab*-planes of the film.

film with the hybrid BZO defect structure has much higher J_c for both field directions and smaller J_c anisotropy compared to all other samples. Similar J_c ($H||c$) versus J_c ($H||ab$) behavior is also observed at 65 K, 3 T (see Figure S2, Supporting Information). The results suggest that the correlated pinning and $J_c(\theta)$ are strongly affected by the manner in which it is incorporated and successfully tuned by controlling *ab*-planes and *c*-axis correlated defect structures individually and simultaneously by material design.

3. Conclusions

In conclusion, a joint experimental, theoretical, and computational study was performed to understand and control the self-assembly of insulating BZO nanophase within high-T_c superconducting films. The size selection and spatial ordering processes of BZO self-assembly were well understood by thermodynamic and kinetic modeling. By tuning the strain in the growing film, the spatial ordering of BZO nanodots inside REBCO matrix was shown to be controllable. The strong correlation between critical current density (J_c) and the alignment of BZO defects landscape was observed. When BZO nanodots are preferentially aligned both parallel and perpendicular to the *c*-axis of REBCO, simultaneously, synergetic enhancement in the pinning and J_c over all magnetic field angles is observed. Results obtained in this study are applicable to other material system combinations and could have a broad impact for ordered nanostructures of one multication material in another multication material for a wide range of applications.

4. Experimental Section

The multilayer films, $[NdBCO_{x\text{u.c.}}/BZO_{y\text{u.c.}}] \times N$, with different unit cell thicknesses of NdBCO and BZO layers are grown by sequential deposition process using pulsed laser deposition (PLD) with a KrF laser ($\lambda = 248$ nm) at repetition rates of 5–10 Hz. Laser ablation of each layer and target rotation were automatically controlled by a computer. Prior to the deposition, the growth rates of NdBCO and BZO layers were confirmed to achieve accurate thickness control of the multilayer films. Laser energy density and substrate to target distance were fixed to 1.5 J cm^{-2} and 7 cm, respectively. Films were grown at a substrate temperature (T_s) of 780 °C in 1%O_2/Ar gas at a deposition pressure of 800 mTorr. All depositions were performed on ion-beam-assisted deposition (IBAD)-MgO templates with a $LaMnO_3$ cap layer that were supplied from Superpower, Inc. The $[(NdBCO+2\%\text{-}BZO)_{3\text{u.c.}}/BZO_{0.5\text{u.c.}}]$ samples with a hybrid BZO defect structure were also grown by sequential ablation of NdBCO+2%-BZO and BZO targets. In this case the NdBCO target containing 2 vol% BZO powder produced 3D self-assembled stacks of BZO nanodot arrays aligned along the *c*-axis while BZO pseudo-layer produced BZO nanodots arrays aligned to the *ab*-planes of the film. After deposition, samples were in situ annealed at T_s = 500 °C and $P(O_2)$ = 500 Torr for 30 min, and ex situ annealed at 500 °C for 1 h in flowing O_2 gas after depositing sputtered Ag electrodes onto the films. The standard four-point probe method was used for the transport measurements including T_c and J_c with a voltage criterion of 1 μV cm^{-1}. Cross-sectional microstructures were characterized by transmission electron microscopy using a Hitachi HF-3300 TEM/STEM with a secondary detector and an energy-dispersive X-ray spectrometer at 300 kV. TEM cross-section specimens were prepared using the focused-ion beam (FIB) technique.

Supporting information

Supporting Information is available from the Wiley Online Library or from the author.

Acknowledgements

The authors thank V. Selvamanickam at SuperPower Inc. for providing the Hastelloy substrates with an IBAD MgO layer/ Homoepitaxial MgO layer/ Epitaxial $LaMnO_3$. This research was sponsored by US Department of Energy, Office of Electricity Delivery and Energy Reliability (DOE-OE) and by the Laboratory Directed Research and Development (LDRD) funds. Y.G., J.M., J.Z., and G.M.S. were supported by LDRD funds, S.H.W. was supported by DOE-OE, and A.G. was supported jointly by DOE-OE and LDRD funds. A portion of this research was conducted at the SHaRE User Facility, which is sponsored by the Division of Scientific User Facilities, Office of Basic Energy Sciences, U.S. Department of Energy.

Received: October 12, 2012
Published online: November 12, 2012

[1] H. Zheng, J. Wang, S. E. Lofland, Z. Ma, L. Mohaddes-Ardabili, T. Zhao, L. Salamanca-Riba, S. R. Shinde, S. B. Ogale, F. Bai, D. Viehland, Y. Jia, D. G. Schlom, M. Wuttig, A. Roytburd, R. Ramesh, *Science* **2004**, *303*, 661.
[2] M. Jamet, A. Barski, T. Devillers, V. Poydenot, R. Dujardin, P. Bayle-Guillemaud, J. Rothman, E. Bellet-Amalric, A. Marty, J. Cibert, R. Mattana, S. Tatarenko, *Nat. Mater.* **2006**, *5*, 653.
[3] L. Mohaddes-Ardabili, H. Zheng, S. B. Ogale, B. Hannoyer, W. Tian, J. Wang, S. E. Lofland, S. R. Shinde, T. Zhao, Y. Jia, L. Salamanca-Riba, D. G. Schlom, M. Wuttig, R. Ramesh, *Nat. Mater.* **2004**, *3*, 533.
[4] T. C. Harman, P. J. Taylor, M. P. Walsh, B. E. LaForge, *Science* **2002**, *297*, 2229.
[5] A. Goyal, US Patent 8034745, **2011**.
[6] A. Goyal, S. Kang, K. J. Leonard, P. M. Martin, A. A. Gapud, M. Varela, M. Paranthaman, A. O. Ijaduola, E. D. Specht, J. R. Thompson, D. K. Christen, S. J. Pennycook, F. A. List *Supercond. Sci. Technol.* **2005**, *18*, 1533.
[7] S. Kang, A. Goyal, J. Li, A. A. Gapud, P. M. Martin, L. Heatherly, J. R. Thompson, D. K. Christen, F. A. List, M. Paranthaman, D. F. Lee, *Science* **2006**, *311*, 1911.
[8] S. H. Wee, A. Goyal, Y. L. Zuev, S. Cook, L. Heatherly, *Supercond. Sci. Technol.* **2007**, *20*, 789.
[9] P. MeleK. Matsumoto, T. Horide, A. Ichinose, M. Mukaida, Y. Yoshida, S. Horii, R. Kita, *Supercond. Sci. Technol.* **2008**, *21*, 032002.
[10] S. H. Wee, A. Goyal, Y. L. Zuev, C. Cantoni, V. Selvamanickam, E. D. Specht, *Appl. Phys. Exp.* **2010**, *3*, 023101.
[11] S. H. Wee, A. Goyal, E. D. Specht, C. Cantoni, Y. L. Zuev, V. Selvamanickam, S. Cook, *Phys. Rev. B* **2010**, *81*, 140503.
[12] X. Qianghua, A. Madhukar, P. Chen, N. P. Kobayashi, *Phys. Rev. Lett.* **1995**, *75*, 2542.
[13] A. Goyal, 2009 Annual Peer Review for the U.S. Superconductivity Program for Electric Systems, Washington, DC **2009** (unpublished).
[14] J. D. Eshelby, *Proc. R. Soc. London, Ser. A* **1957**, *241*, 376.
[15] W. Pompe, X. Gong, Z. Suo, J. S. Speck *J. Appl. Phys.* **1993**, *74*, 6012.
[16] S. Zheng, W. Zhu, Y. F. Gao, G. M. Stocks, Z. Zhang, *Appl. Phys. Lett.* **2010**, *96*, 071913.
[17] Y. F. Gao, W. Lu, Z. Suo, *Acta Mater.* **2002**, *50*, 2297.
[18] J. Zhang, K. Zhang, J. Zhong, *Appl. Phys. Lett.* **2004**, *84*, 1853.
[19] S. H. Wee, A. Goyal, J. Li, Y. L. Zuev, S. Cook, *J. Appl. Phys.* **2007**, *102*, 063906.
[20] H. Yang, H. Wang, B. Maiorov, J. Lee, D. Talbayev, M. J. Hinton, D. M. Feldmann, J. L. Macmanus-Driscoll, A. J. Taylor, L. Civale, T. R. Lemberger, Q. X. Jia, *J. Appl. Phys.* **2009**, *106*, 093914.